Spiraling anomalous vortex beam arrays in strongly nonlocal nonlinear media

Limin Song, Zhenjun Yang,* Shumin Zhang, and Xingliang Li
College of Physics and Information Engineering, Hebei Advanced Thin Films Key Laboratory, Hebei Normal University, Shijiazhuang 050024, China

(Received 22 January 2019; published 12 June 2019)

We introduce a class of spiraling anomalous vortex beam (AVB) arrays in strongly nonlocal nonlinear media. The general analytical formula for the arrays is derived, and its propagation properties are analyzed. It is shown that the spiraling AVB arrays can present three different propagation states (shrink, expansion, and the dynamical bound state) depending on the absolute value of the transverse velocity parameter ($0 < |\xi| < 1$, $|\xi| > 1$, and $|\xi| = 1$). Accordingly, we propose the concept of array breathers and array solitons. The topological charge of the vortex and the number of the constituent AVB also play important roles in the evolution of the AVB arrays. It is found that the light intensity of the central region of the array's field under an in-phase incident condition is not zero during propagation if and only if the ratio between the two parameters is an integer. By using the derived analytical expression, a series of numerical examples is exhibited to graphically illustrate these typical propagation properties. In addition, we give a variety of array forms of multibeam interaction. Our results may provide insight into vortex beam arrays and may be applied in optical communication and particle control.

DOI: 10.1103/PhysRevA.99.063817

I. INTRODUCTION

Spatial beam propagation in nonlocal nonlinear media has sparked considerable interest both theoretically and experimentally, especially in strongly nonlocal nonlinear media (SNNM), such as nematic liquid crystals [1,2] and lead glasses [3–5]. In the physical settings of strongly nonlocality, the characteristic range of the response function of the medium is much larger than the space occupied by the beam; the nonlinear polarization of the medium at a particular point depends not only on the beam intensity at this position but also on the optical field at a certain space scale [6,7]. This provides a favorable condition for researchers to study the propagation and transformation of spatial beams [8–11]. Lu *et al.* proposed that beam propagation in SNNM can be regarded as a self-induced fractional Fourier transform [12], and when multiple beams propagate in SNNM together each constituent beam can be regarded as a cross-induced fractional Fourier transform [13]. This provides a powerful theoretical basis for studying the propagation properties of multiple beams in SNNM.

In recent years, the subject of vortex beams has become a hot spot due to their unique spiral phase distribution and their notable feature of carrying orbital angular momentum [14–20], both in fundamental and applied physics. The progress in generating vortex beams in nonlinear bulk media opens the possibility to study true interaction of multidimensional vortex waves [21,22]. In SNNM, the natural spreading of vortex beams due to diffraction can be exactly compensated by the self-focusing effect, which is modeled as a dependence of the refractive index on the beam intensity, and thus the vortex soliton can be formed. Spatial vortex solitons (beams) can carry or limit other weaker signals to form light-induced waveguides and thereby control the signal transmission path and output position through their trajectories [6], which has important applications in new mechanisms of interaction between beams and matter, research on optical communication [23], and particle control [24]. As early as 1997, the theory of the motion of spiraling solitons has been proposed [25,26]. The existence of higher-order rotating spatial solitons in nonlocal nonlinear media has been demonstrated [27]. Up to now, various models of multibeam (multisoliton) interaction have been constructed theoretically and some of them have been implemented in experiments, such as soliton clusters [28–31] and soliton pairs [25,32,33]. In this paper, we carry out the basic principles for constructing the so-called spiraling beam arrays and take anomalous vortex beam (AVB) arrays as an example to explore the propagation properties of them in SNNM.

The structure of this paper is designed as follows. In Sec. II, the governing equation of the spiraling AVB array is given by using the equivalent form of the Collins integral formula in SNNM and the superposition principle. In Sec. III, we discuss the propagation properties of the AVB arrays based on propagation expression. The evolution of the intensity pattern, the projection trajectory, and the phase change are discussed in detail by means of mathematical technique. In addition, various beam array forms within the realm of possibility are given in this section. In Sec. IV, we conclude this paper.

II. MODEL EQUATION

The propagation dynamics of a paraxial laser beam in nonlocal nonlinear media can often be described theoretically as an evolution ruled phenomenologically by the nonlocal nonlinear Schrödinger equation (NNLSE) [6–8,12,13,34–36]

$$\frac{\partial \Phi}{\partial z} = \frac{i}{2k}\Delta_{\perp}\Phi + ik\frac{\delta n}{n_0}\Phi, \tag{1}$$

*Corresponding author: zjyang@vip.163.com

where Φ is the complex amplitude of the paraxial laser beams; $k = \omega n_0/c$, with ω the circular frequency, is the wave number in the media without nonlinearity; $\Delta_\perp$ is the two-dimensional transverse Laplacian operator; n_0 is the linear part of the refractive index of the media; $\delta n = n_2 \iint R(\mathbf{r}-\mathbf{r}_c)|\Phi(\mathbf{r}_c,z)|^2 d^2\mathbf{r}_c$ is the nonlinear perturbation of the refractive index caused by the beam ($|\delta n| \ll n_0$); n_2 is the nonlinear index coefficient. Thus, the refractive index of nonlocal nonlinear media can be expressed as $n(\mathbf{r}) = n_0 + \delta n(\mathbf{r})$. $\mathbf{r}$ and $\mathbf{r}_c$ represent two-dimensional transverse coordinate vectors, and $R(\mathbf{r})$ is the normalized symmetrical real spatial response function of the media and it satisfies $\iint R(\mathbf{r}) d^2\mathbf{r} = 1$. Equation (1) describes the evolution of a spatial beam trapped in an effective parabolic graded index channel with the profile given by the nonlocal response function $R(\mathbf{r})$, which usually is taken as Gaussian function form $R(\mathbf{r}) = 1/(2\pi w_R^2)\exp[-\mathbf{r}^2/(2w_R^2)]$ [7,35–37], where w_R is the characteristic width of $R(\mathbf{r})$.

In the strongly nonlocal nonlinear limit, the response function $R(\mathbf{r})$ can be expanded into Taylor series, thus the NNLSE can be simplified [7]. If we only expand the response $R(\mathbf{r}-\mathbf{r_c})$, with $\mathbf{r_c} = 0$, to the second-order term, then we obtain

$$\delta n \approx n_2 P_0\left(R_0 + \tfrac{1}{2}R_0''\mathbf{r}^2\right), \tag{2}$$

and Eq. (1) reduces to

$$\frac{\partial \Phi}{\partial z} = \frac{i}{2k}\Delta_\perp \Phi - \frac{ik\gamma^2 P_0 \mathbf{r}^2}{2}\Phi + \frac{ikn_2 R_0 P_0}{n_0}\Phi, \tag{3}$$

where $\gamma = \sqrt{-n_2 R_0''/n_0}$ is a material constant associated with the nonlocal effect of the medium and $\gamma^2 > 0$ corresponds to a focusing nonlinear case [$R_0 = R(\mathbf{0})$, $R_0'' = R''(\mathbf{0})$, $R_0'' < 0$ because R_0 is a maximum of $R(\mathbf{r})$]. $P_0 = \iint |\Phi(\mathbf{r},0)|^2 d^2\mathbf{r}$ is the input power and it is conserved in the process of beam propagation [7]. By introducing the variable transformation

$$\Phi(\mathbf{r},z) = E(\mathbf{r},z)\exp\left(ik\frac{n_2 R_0 P_0}{n_0}z\right), \tag{4}$$

Eq. (3) can be simplified as the famous strongly nonlocal nonlinear model

$$\frac{\partial E}{\partial z} = \frac{i}{2k}\Delta_\perp E - \frac{ik\mathbf{r}^2}{2}\gamma^2 P_0 E. \tag{5}$$

It should be noted here that in the derivation of Eq. (5) we assume that the response function is symmetric and twice differentiable at $x = y = 0$. However, the response function of the actual physical system has no rules to follow, so it cannot be simply transformed into the strongly nonlocal nonlinear model. However, the strongly nonlocal nonlinear model retains the main features of SNNM, and the physical characteristics do not intensively depend on the form of the response function as long as the nonlocality of the media is strong enough [38].

The center of mass $\mathbf{r}_c$ of a single beam traveling in a parabolic graded index medium satisfies the paraxial ray equation [6,39]

$$\frac{d}{dl}\left(n\frac{d\mathbf{r}_c}{dl}\right) = \nabla n, \tag{6}$$

where l is the length of the center of mass of the beam from one point to another, $\mathbf{r}_c$ is the position vector of that point, and ∇ is the gradient operator. Under paraxial approximation, $dl \approx dz$. Therefore, Eq. (6) can be rewritten as

$$\frac{d}{dz}\left(n\frac{d\mathbf{r}_c}{dz}\right) = \nabla n, \tag{7}$$

and then

$$\frac{dn}{dz}\left(\frac{d\mathbf{r}_c}{dz}\right) + n\left(\frac{d^2\mathbf{r}_c}{dz^2}\right) = \nabla n. \tag{8}$$

In self-focusing nonlocal media the refractive index only has a transverse distribution and thus $dn/dz = 0$. Therefore, Eq. (6) can be reduced as an ordinary differential equation

$$\frac{d^2\mathbf{r}_c}{dz^2} = -\frac{\mathbf{r}_c}{z_p^2}, \tag{9}$$

which describes the trajectory of the center of mass of a beam in SNNM. $z_p = (\gamma^2 P_0)^{-1/2}$ is a parameter related to the properties of materials and the input power. One can obtain the solution of Eq. (9) as

$$\mathbf{r}_c(z) = \mathbf{r}_c(0)\cos\left(\frac{z}{z_p}\right) + z_p\mathbf{r}_c'(0)\sin\left(\frac{z}{z_p}\right). \tag{10}$$

Here, the superscript "′" represents the first derivative, and it can be proved that if $E(\mathbf{r},z)$ is a solution of Eq. (5) then so is

$$E_\pm(\mathbf{r},z) = E(\mathbf{r} \pm \mathbf{r}_c(z), z)\exp[\mp i\boldsymbol{u}(z)\mathbf{r} + i\phi(z)], \tag{11}$$

where $\boldsymbol{u}(z)$ and $\phi(z)$ are determined by the following equations:

$$\boldsymbol{u}(z) = k\mathbf{r}_c'(z), \tag{12}$$

$$\phi'(z) = \frac{k}{2}\left[\frac{\mathbf{r}_c^2(z)}{z_p^2} - \mathbf{r}_c'^2(z)\right]. \tag{13}$$

In the cylindrical coordinates system, the z axis is taken to be the propagation axis. The AVB in the source plane $z = 0$ takes the ansatz form as [21]

$$E(r_0,\theta_0,0) = E_0\left(\frac{r_0}{w_0}\right)^{2n+|m|}\exp\left(-\frac{r_0^2}{w_0^2}\right)\exp(-im\theta_0), \tag{14}$$

where $E_0 = \{2^{2n+m+1}P_0/[\pi w_0^2\Gamma(2n+m+1)]\}^{1/2}$ is a normalized coefficient to ensure that the input power equals P_0, $\Gamma(\cdot)$ is the Euler gamma function, $n\,(=0,1,2,\ldots)$ is the beam order of the AVB, $m\,(=0,\pm1,\pm2,\ldots)$ is the topological charge of the vortex and it is also the orbital angular momentum quantum number, w_0 is the beam waist size of the corresponding fundamental Gaussian beam ($m = n = 0$) in transverse space, and r_0 and θ_0 are radial and azimuthal coordinates, respectively. When $m = 0$ and $n \neq 0$, Eq. (14) can be used to characterize the electric field of a hollow Gaussian beam [40]. When $m \neq 0$ and $n = 0$, Eq. (14) can be used to characterize the electric field of an ordinary Gaussian vortex beam, i.e., a $(0, m)$ mode Laguerre-Gaussian beam [34]. Thereout, the AVB is an important beam type in that it can generalize several beams.

In theory, one can investigate the propagation of the AVB in SNNM based on Eqs. (5) and (14) directly. However, it is almost impossible to analytically obtain the propagation expression of the AVB by reason of the complication in mathematical calculations. Luckily, in the strongly nonlocal nonlinear limit, the beam propagation can be solved based on the matrix optics and the fractional Fourier transform [12,41]. Therefore, the analytical expression of the AVB propagating in SNNM can be treated by the Collins integral formula with the following form:

$$E(r,\theta,z) = -\frac{ik}{2\pi z_p \sin(z/z_p)} \exp\left[\frac{ikr^2}{2z_p \tan(z/z_p)}\right] \int_0^{2\pi}\int_0^{\infty} E(r_0,\theta_0,0) \exp\left[\frac{ikr_0^2}{2z_p \tan(z/z_p)} - \frac{2ikrr_0\cos(\theta-\theta_0)}{z_p \sin(z/z_p)}\right] r_0 dr_0 d\theta_0, \tag{15}$$

where the phase factor $\exp(-ikz)$ is ignored for brevity. The propagation expression of a single AVB in SNNM can be obtained by substituting Eq. (14) into Eq. (15) and with the aid of the following integral formulas [42]:

$$\int_0^{2\pi} \exp[-in\theta_1 + ikbr\cos(\theta_1-\theta_2)]d\theta_1 = 2\pi \exp\left[in\left(\frac{\pi}{2}-\theta_2\right)\right] J_n(kbr), \tag{16}$$

$$\int_0^{\infty} \exp(-ax^2) J_v(2bx) x^{2n+v+1} dx = \frac{n!}{2} b^v a^{-(n+v+1)} \exp\left(-\frac{b^2}{a}\right) L_n^v\left(\frac{b^2}{a}\right), \tag{17}$$

where $J_v(\cdot)$ is the Bessel function and $L_n^v(\cdot)$ are the generalized Laguerre polynomials. After some complicated integral calculations, one can obtain the propagation expression as

$$E(r,\theta,z) = \frac{i^{|m|+1} E_0 n! z_r}{z_p \sin(z/z_p)} \left[\frac{z_r r}{w_0 z_p \sin(z/z_p)}\right]^{|m|} \left[1 + \frac{iz_r}{z_p \tan(z/z_p)}\right]^{-(n+|m|+1)} \exp\left\{-\frac{z_r^2 r^2}{[z_p + iz_r \sin(z/z_p)] w_0^2 z_p \sin^2(z/z_p)}\right\}$$
$$\times \exp\left\{-\frac{iz_r r^2}{w_0^2 z_p \tan(z/z_p)}\right\} L_n^{|m|}\left\{\frac{z_r r^2}{[z_p + iz_r \cot(z/z_p)] w_0^2 z_p \sin^2(z/z_p)}\right\} \exp(-im\theta). \tag{18}$$

What follows is the construction of the AVB arrays. We consider a coherent superposition of N AVBs; then the slowly varying field envelope of the AVB arrays can be expressed as

$$\Phi(r,\theta,z) = A_0 \sum_{j=1}^{N} E_j(r,\theta,z), \tag{19}$$

where A_0 is the normalized amplitude of the total input field and E_j is the light field of the jth AVB. Whereas two-dimensional transverse coordinate vector $\mathbf{r} = x\mathbf{e}_x + y\mathbf{e}_y$ in the Cartesian coordinates system, it has the following transformation relationship in the cylindrical coordinates system:

$$\mathbf{r} = (x,y) = (r\cos\theta, r\sin\theta) = (r,\theta). \tag{20}$$

Combining the equations above and with the aid of Euler equation $e^{i\theta} = \cos\theta + i\sin\theta$, the propagation expression of each constituent AVB in the Cartesian coordinate system can be rewritten as

$$E_j(x,y,z) = \frac{i^{|m|+1} E_0 n! z_r}{z_p \sin(z/z_p)} \left[\frac{z_r\sqrt{(x-x_{cj})^2 + (y-y_{cj})^2}}{w_0 z_p \sin(z/z_p)}\right]^{|m|} \left[1 + \frac{iz_r}{z_p \tan(z/z_p)}\right]^{-(n+|m|+1)}$$
$$\times \exp\left\{-\frac{(z_r^2/z_p)[(x-x_{cj})^2 + (y-y_{cj})^2]}{[z_p + iz_r \sin(z/z_p)] w_0^2 \sin^2(z/z_p)}\right\} \exp\left\{-\frac{iz_r[(x-x_{cj})^2 + (y-y_{cj})^2]}{w_0^2 z_p \tan(z/z_p)}\right\}$$
$$\times L_n^{|m|}\left\{\frac{(z_r/z_p)[(x-x_{cj})^2 + (y-y_{cj})^2]}{[z_p + iz_r \cot(z/z_p)] w_0^2 \sin^2(z/z_p)}\right\} \left[\frac{(x-x_{cj}) - i(y-y_{cj})}{\sqrt{(x-x_{cj})^2 + (y-y_{cj})^2}}\right]^{|m|} \exp[i(u_{xj}\cdot x + u_{yj}\cdot y + \phi_j)], \tag{21}$$

where $z_r = kw_0^2/2$ is the Rayleigh length of the fundamental Gaussian beam; $z_p = \sqrt{P_{gc}/P_0} z_r$ is a normalized propagation distance associated with the input power; $P_{gc} = 1/(\gamma^2 z_r^2)$ is the soliton power for a Gaussian beam in SNNM [7]. Considering the independence of variables in x and y directions and combining Eqs. (10)–(13), Eq. (21) is expressed as

$$x_{cj}(z) = c_{xj}\cos\left(\frac{z}{z_p}\right) + t_{xj} z_p \sin\left(\frac{z}{z_p}\right), \tag{22}$$

$$y_{cj}(z) = c_{yj}\cos\left(\frac{z}{z_p}\right) + t_{yj} z_p \sin\left(\frac{z}{z_p}\right), \tag{23}$$

which jointly govern the trajectory of the center of mass of each constituent AVB, and

$$u_{xj}(z) = -\frac{kc_{xj}}{z_p}\sin\left(\frac{z}{z_p}\right) + kt_{xj}\cos\left(\frac{z}{z_p}\right), \tag{24}$$

$$u_{yj}(z) = -\frac{kc_{yj}}{z_p}\sin\left(\frac{z}{z_p}\right) + kt_{yj}\cos\left(\frac{z}{z_p}\right), \tag{25}$$

$$\phi_j(z) = \frac{k}{4}\left[\frac{c_{xj}^2 + c_{yj}^2}{z_p} - z_p\left(t_{xj}^2 + t_{yj}^2\right)\right]\sin\left(\frac{2z}{z_p}\right) - \frac{k}{2}\left(c_{xj}t_{xj} + c_{yj}t_{yj}\right)\cos\left(\frac{2z}{z_p}\right). \tag{26}$$

In all of the above equations, $c_{xj} = x_{cj}(z)|_{z=0}$ and $c_{yj} = y_{cj}(z)|_{z=0}$ are the initial transverse coordinates (initial position) of the center of mass of each AVB; $t_{xj} = x'_{cj}(z)|_{z=0}$ and $t_{yj} = y'_{cj}(z)|_{z=0}$ are the slopes of the projection trajectory of each beam center on the x-z plane and y-z plane, named as "initial transverse velocity," indicating the size of the angle between the incident direction and the propagation axis. We borrow the concept of "initial transverse velocity" from classical physics. That is, the propagation distance z is regarded as time t, and then the first derivative of position vector $\mathbf{r}_c$ to time z is velocity. The term "initial transverse velocity" is very convenient to help us understand the propagation of the beam. Of course, we can also call it the "initial incident slope." Then the angle between the projection of the incident direction vector on the x-z (or y-z) plane and the propagation axis is $\Lambda_{xj} = \arctan(t_{xj})$ [or $\Lambda_{yj} = \arctan(t_{yj})$]. We can define the angle Λ as the initial tilted angle, and in the case of strong nonlocality Λ can approach 90 deg in theory [43].

Consider a simple configuration in which the AVB arrays are arranged in a ringlike geometry with radius r and launched with a fixed difference between adjacent beams. Then, the position of each constituent AVB center can be taken as

$$c_{xj} = r\cos\varphi_j, \quad c_{yj} = r\sin\varphi_j, \tag{27}$$

and the initial transverse velocity of each AVB can be expressed as

$$t_{xj} = -\frac{\xi r\sin\varphi_j}{z_p}, \quad t_{yj} = \frac{\xi r\cos\varphi_j}{z_p}, \tag{28}$$

where $\varphi_j = 2j\pi/N$ $(j = 1, 2, \ldots, N)$ is the angle between the center of the corresponding AVB and the x axis, and ξ is defined as "transverse velocity parameter." If $\xi = 0$, it is the general case and the interacting beams are periodic collisions in the form of a simple harmonic oscillator [6,44], which does not rotate and is well understood. We mainly study the case of $\xi \neq 0$ in this paper, i.e., every constituent AVB is launched with a twisted trajectory at the source plane.

III. PROPAGATION PROPERTIES

A. Three different propagation states

The propagation expression [Eq. (21)] derived here is not the exact solution to the NNLSE, but an approximate one. However, it is sufficient to characterize the propagation and transformation of spatial beams in that it agrees well with the exact solution of the NNLSE in the strongly nonlocal nonlinear case, i.e., Eq. (5) [12,41]. We introduce a parameter μ to describe the degree of nonlocality of the media and define $\mu = w_R/w_B$, where w_B is the second-order moment width of the combined optical field. We have compared various analytical solutions of the strongly nonlocal nonlinear model with the exact results of numerical simulation of the NNLSE for different nonlocality degrees. It shows that with the increase of μ the analytical solutions become better approximations of the exact numerical results of the NNLSE especially when $\mu \geqslant 10$. Next, we mainly discuss the propagation properties of AVB arrays in SNNM based on the analytical solutions.

Some interesting phenomena regarding the AVB arrays are shown when the general analytical formula is considered. It is found that the evolution of the AVB arrays is periodic, with the period $\Delta z_t = 2\pi z_p$ depending on the input power P_0. The center of mass of the AVB array is always located at the z axis in that the total transverse spatial momentum [13]

$$\mathbf{M}_\perp = \frac{i}{2k}\iint(\Phi\nabla_\perp\Phi^* - \Phi^*\nabla_\perp\Phi)dxdy \equiv \mathbf{0}, \tag{29}$$

where $\nabla_\perp = \mathbf{e}_x\partial_x + \mathbf{e}_y\partial_y$ and the asterisk denotes the complex conjugate. The distance from the center of each constituent beam to the propagation axis can be obtained as

$$d_j(z) = r\left[\cos^2\left(\frac{z}{z_p}\right) + \xi^2\sin^2\left(\frac{z}{z_p}\right)\right]^{1/2} \tag{30}$$

based on Eqs. (22) and (23). The same propagation constant ensures that the beam array is a regular N-sided shape at any cross section during propagation. One can obtain the area around the N-sided-shaped beam array as

$$S = \frac{Nr^2}{2}\left[\cos^2\left(\frac{z}{z_p}\right) + \xi^2\sin^2\left(\frac{z}{z_p}\right)\right]\sin\left(\frac{2\pi}{N}\right). \tag{31}$$

The angular velocity of each constituent beam is

$$\omega_j(z) = \frac{\xi/z_p}{\cos^2\left(\frac{z}{z_p}\right) + \xi^2\sin^2\left(\frac{z}{z_p}\right)}. \tag{32}$$

Because of the synchronism of the motion of each constituent beam, we can eliminate the subscript j in Eqs. (30) and (32) and record the equations directly as $d(z)$ and $\omega(z)$, respectively, in the discussion that follows.

Figure 1 illustrates the effect of the transverse velocity on the AVB arrays during propagation. One sees that if $\xi = 1$ [Figs. 1(b1)–1(b5)] the size of the AVB array remains invariant intuitively, though it rotates while propagating. This can be verified by Eq. (31), when $\xi = 1$ and $S \equiv$ const. And the corresponding projection trajectory in the x-y plane is a circle [solid line in Fig. 1(f)], which has its own equation:

$$x^2 + y^2 = r^2. \tag{33}$$

If $0 < \xi < 1$ ($\xi > 1$), the size of the AVB array evolves to be smaller (larger) first and then larger (smaller) periodically, and the minimum (maximum)

$$S_{\min(\max)} = \frac{N\xi^2r^2}{2}\sin\left(\frac{2\pi}{N}\right) \tag{34}$$

appears at $z = (p + 1/2)\pi z_p$ $(p = 0, 1, 2, \ldots)$. Each constituent AVB spirals inward and outward simultaneously, as

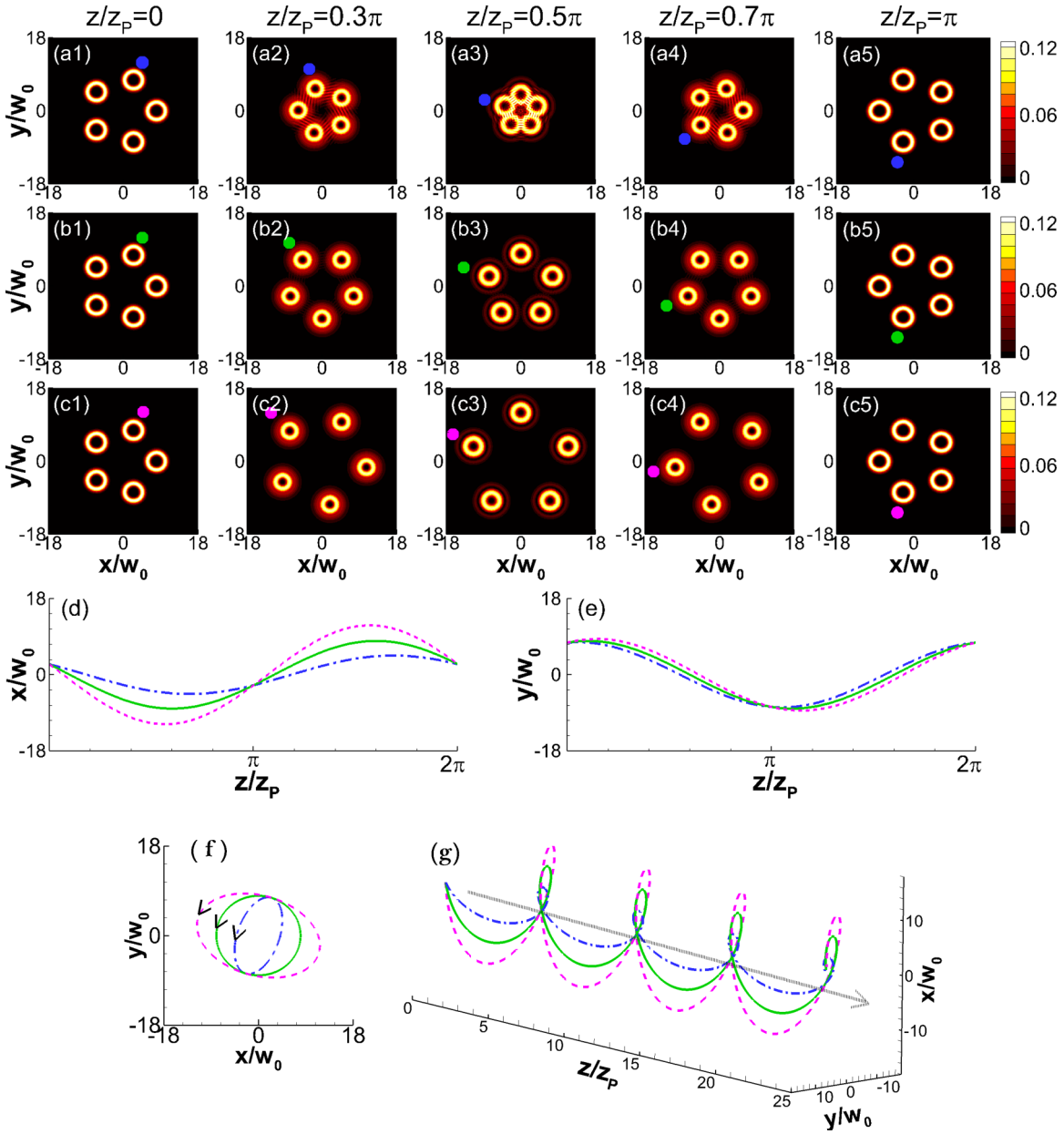

FIG. 1. Different regimes of the interaction of the AVB arrays. (a–c) Transverse intensity patterns at different propagation positions. Marked with a circle is E_1; the counterclockwise direction is followed by E_2, E_3, E_4, and E_5 successively. The same parameters are chosen as $N = 5$, $m = n = 3$, $r = 8w_0$, $P_0 = P_{gc}/5$. The transverse velocity parameters are taken as $\xi = 1/2$, $\xi = 1$, $\xi = 3/2$, corresponding to (a)–(c), respectively. (d, e) The projection trajectories of E_1 in the x-z plane and y-z plane, respectively. (f) The projection trajectories of E_1 in the x-y plane with different transverse velocity parameters; the arrows indicate the direction of motion. (g) Three-dimensional propagation trajectories of E_1; the line with an arrow indicates the propagation axis and points out the direction of propagation. The velocity parameters are taken as $\xi = 1/2$ for the dash-dotted line, $\xi = 1$ for the solid line, and $\xi = 3/2$ for the dashed line, respectively.

shown in Figs. 1(a) and 1(c), and the corresponding projection trajectory in the x-y plane is an ellipse with the equation

$$(\xi^2\cos^2\varphi_j + \sin^2\varphi_j)x^2 + (\xi^2\sin^2\varphi_j + \cos^2\varphi_j)y^2 + [(\xi^2-1)\sin(2\varphi_j)]xy = \xi^2 r^2, \tag{35}$$

[see dash-dotted and dashed lines in Fig. 1(f)]. For clarity, only the projection trajectories of E_1 are given in Figs. 1(d)–1(f); other constituent AVBs are similar to this. One can find from Fig. 1(f) that, other things beimg equal, the short axis (long axis) of the ellipse when $\xi > 1$ ($\xi < 1$) is externally (internally) tangential to the circular projection trajectory when $\xi = 1$. Additionally, whatever the value of ξ, the projection trajectories of each constituent beam in the x-z plane and y-z plane always change sinusoidally, which indicates that every interacting beam undergoes a twisted trajectory that oscillates around the propagation axis. The corresponding projection trajectories in the x-z plane and y-z plane can be described as

$$x_{cj}(z) = \frac{r}{2}[(1-\xi)\cos\alpha + (1+\xi)\cos\beta] \tag{36}$$

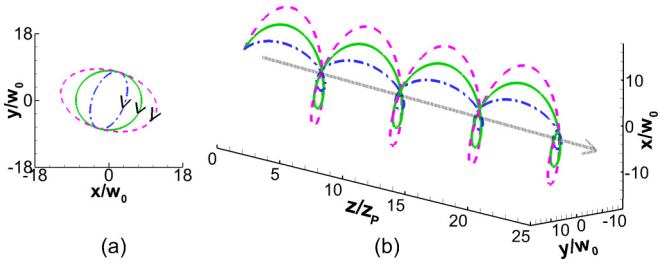

FIG. 2. The same as Figs. 1(f) and 1(g) except that the velocity parameters are taken as $\xi = -1/2$ for the dash-dotted line, $\xi = -1$ for the solid line, and $\xi = -3/2$ for the dashed line, respectively.

and

$$y_{cj}(z) = \frac{r}{2}[(1-\xi)\sin\alpha + (1+\xi)\sin\beta], \tag{37}$$

respectively, with the auxiliary parameters $\alpha = \varphi_j - z/z_p$ and $\beta = \varphi_j + z/z_p$. Note that $P_0 = P_{gc}/5$ is the critical power of a single AVB for $m = n = 3$ [45]. While it ensures that the second-order moment width of each constituent AVB remains invariant during propagation, the intensity patterns of the beams are variable due to the carried orbital angular momentum. The three ranges ($0 < \xi < 1$, $\xi > 1$, and $\xi = 1$) of the transverse velocity parameter correspond to the three states (shrink, expansion, and dynamical bound state) of beam array propagation.

In Figs. 1(f) and 1(g), we give the three-dimensional propagation trajectories and the projection trajectories in the x-y plane of E_1 for different velocity parameters. We can see that the constituent beams interact with each other in a spiraling motion with elliptical or circular orbits in the same period. When $\xi > 1$ ($0 < \xi < 1$), the constituent AVB is away from (close to) the propagation axis first and then close to (away from) the propagation axis, but when $\xi = 1$ its distance to the propagation axis is invariant from beginning to end. This not only is intuitively observed from Fig. 1 but also can be proved strictly from Eq. (30). It can be seen that each constituent beam revolves counterclockwise around the propagation axis. The parameters in Figs. 2(a) and 2(b) are the same as those in Fig. 1 except that the velocity parameters are taken as corresponding negative values. Each constituent beam revolves clockwise around the propagation axis at this time. Combining Eq. (32) one can come to the conclusion that if $\xi > 0$ ($\xi < 0$) then the angular velocity $\omega(z) > 0$ [$\omega(z) < 0$], and each constituent beam has a counterclockwise (clockwise) rotation around the propagation axis when it travels along the z axis. Furthermore, if two beam arrays only have differences in signs for velocity parameters, the propagation properties between them are the same except in the opposite direction of rotation. We can calculate the eccentricity of the elliptical trajectory as

$$e = \begin{cases} (1-|\xi|^2)^{1/2}, & 0 < |\xi| < 1, \\ 0, & |\xi| = 1, \\ (1-1/|\xi|^2)^{1/2}, & |\xi| > 1, \end{cases} \tag{38}$$

and its varying curve is shown in Fig. 3. As is well known, the closer the eccentricity gets to 1, the thinner the elliptical trajectory becomes; the closer the eccentricity gets to zero, the closer the elliptical trajectory gets to a circle. In

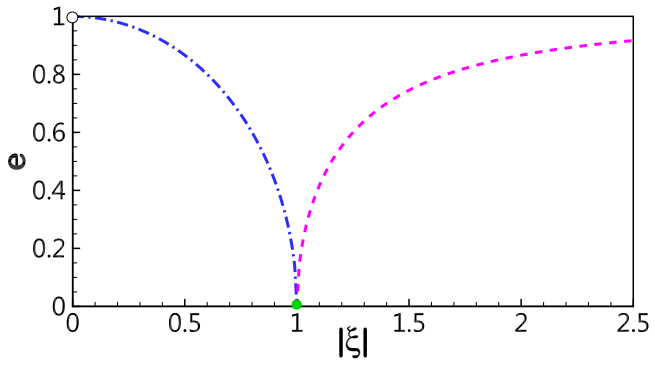

FIG. 3. The eccentricity of elliptical trajectory changes with the velocity parameter.

Eq. (38), the expression of the absolute value of the velocity parameter is determined by

$$|\xi| = \frac{z_p}{r}\sqrt{t_{xj}^2 + t_{yj}^2}. \tag{39}$$

Figure 4 shows the evolution behavior of the array's size for several values of transverse velocity parameter ξ. The other parameters are chosen to be the same as in Fig. 1. In the case of $\xi > 1$ ($0 < \xi < 1$), the size of the AVB array is always larger (smaller) than that in the case of $\xi = 1$, and it breathes with the period $\Delta z_s = \pi z_p$. For that matter, the evolution of the array's size described by Eq. (31) has similar propagation behaviors to the second-order moment width of a single AVB [45]. Thus, we can name these two propagation states as "array breathers." We search the first derivative of Eq. (31) and take the resulting sign-dependent terms as transform parameter κ_S such that

$$\kappa_S = (\xi^2 - 1)\sin\left(\frac{2z}{z_p}\right), \tag{40}$$

and its curve is shown in Fig. 4(b). One sees that, if $\xi > 1$, κ_S is positive within the interval $0 \leqslant z \leqslant \Delta z_s/2$ and negative within the interval $\Delta z_s/2 \leqslant z \leqslant \Delta z_s$; when $0 \leqslant z \leqslant \Delta z_s/4$ and $3\Delta z_s/4 \leqslant z \leqslant \Delta z_s$, the transform parameter increases with increasing the axial propagation distance; when $\Delta z_s/4 \leqslant z \leqslant 3\Delta z_s/4$, the transform parameter decreases with increasing the axial propagation distance [see dashed line in

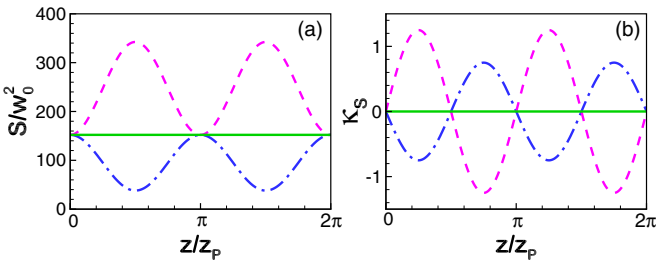

FIG. 4. (a) The size of the AVB array vs propagation distance z for different values of transverse velocity parameter ξ. (b) The transform parameter vs propagation distance. Dash-dotted line, $\xi = 1/2$; solid line, $\xi = 1$; dashed line, $\xi = 3/2$. Parameters: $N = 5$, $m = n = 3$, $r = 8w_0$, $P_0 = P_{gc}/5$.

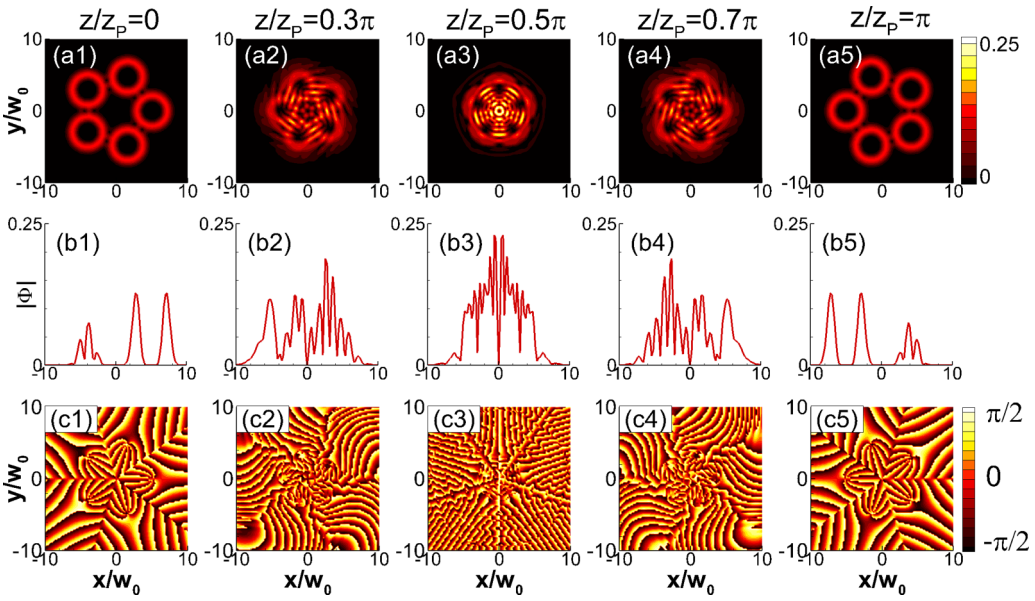

FIG. 5. (a) Transverse intensity patterns at different propagation positions shown at the top. (b) Transverse intensity distributions in the x direction. (c) Phase distributions vs propagation distance. Phase images are scaled from $-\pi/2$ to $\pi/2$. Parameters: $N = 5$, $m = n = 3$, $r = 5w_0$, $\xi = 1/2$, $P_0 = P_{gc}/5$.

Fig. 4(b)]. If $\xi < 1$, the variation of the transform parameter is just the opposite of that when $\xi > 1$ [see dash-dotted line in Fig. 4(b)]. The positive (negative) κ_S indicates that each constituent AVB is in centrifugal (centripetal) motion, and the corresponding S is getting bigger (smaller). Of course, if $\kappa_S \equiv 0$, i.e., $\xi = 1$, this means that the array's size remains invariant as a function of propagation distance z. Correspondingly, we name this propagation state as an "array soliton."

The physical reasons for the above phenomena can be explained as follows. Two beams interacting in a local medium attract each other when they are in phase and repel each other when they are out of phase; two beams interacting in a strongly nonlocal medium, no matter what the phase is between them, always attract each other [6]. Qualitatively, the centrifugal force is inversely proportional to the square of the beam spacing. When $\xi < 1$, the attractive force among the constituent AVBs, which leads to the centripetal motion, is weaker than the centrifugal force induced by the transverse velocity at the initial position; as a result, the AVB array is expanded at the beginning of propagation. Then, as the beam spacing becomes wider, the centrifugal force becomes weaker and weaker. When the beam spacing reaches its maximum, the centrifugal force is already weaker than the attractive force; the beam array is beginning to be compressed and the beam spacing is getting narrower gradually. Thus, under the competition between attractive force and centrifugal force, the array's size varies periodically during propagation. If $\xi > 1$, the array's size also varies periodically except that it is always expanded, not compressed (relative to the case of $\xi = 1$), in that the bigger transverse velocity provides a stronger centrifugal force. Specially, if $\xi = 1$, the centrifugal force is exactly balanced by attractive force due to the beam interaction, so the array's size is neither expanded nor compressed.

B. The influences of topological charge and the number of the constituent AVB on light intensity

From Fig. 1(a), we can see that when transverse velocity or the radius of the ringlike structure is small the transverse light intensity distribution pattern of the AVB array will become more complex due to the correlation and interference effects among the constituent beams. In the following, therefore, we are going to discuss the intensity patterns of the AVB arrays in detail numerically, by using the analytical propagation expression derived above.

A stack of images taken in Fig. 5 illustrates the typical evolution of the AVB arrays in SNNM when $0 < \xi < 1$. It can be seen that although there are many energy peaks around the center of the array field during propagation the central intensity of the array field is always zero, as shown in Figs. 5(a) and 5(b). Based on the propagation expression, we have obtained a complete evolution period of the array as $\Delta z_t = 2\pi z_p$. Here only the first half period (from $z = 0$ to πz_p) is given as follows from the fact that the second half period (from $z = \pi z_p$ to $2\pi z_p$) is a reverse process of the first half period. That is to say, the AVB arrays can be revivable at the end of each evolution period. This is similar to the propagation properties of high-order temporal solitons (or breathers) in nonlinear fiber [46]. One sees that Figs. 5(a) and 5(b) are perfectly symmetric with respect to $z = 0.5\pi z_p$. However, the images in Fig. 5(c) are complementary with respect to $z = 0.5\pi z_p$. If we take one point on each side of the line $z = 0.5\pi z_p$, the distance between them and the line is equal, and we record them as a and b, respectively. Then their phases satisfy the relation $\phi_a + \phi_b = 0$.

Figure 6 presents the evolution of AVB arrays with the same initial parameters as Fig. 5 except that the topological charge is taken as $m = 5$. Most of the features of this rotating array field are the same as those in Fig. 5, but now the central

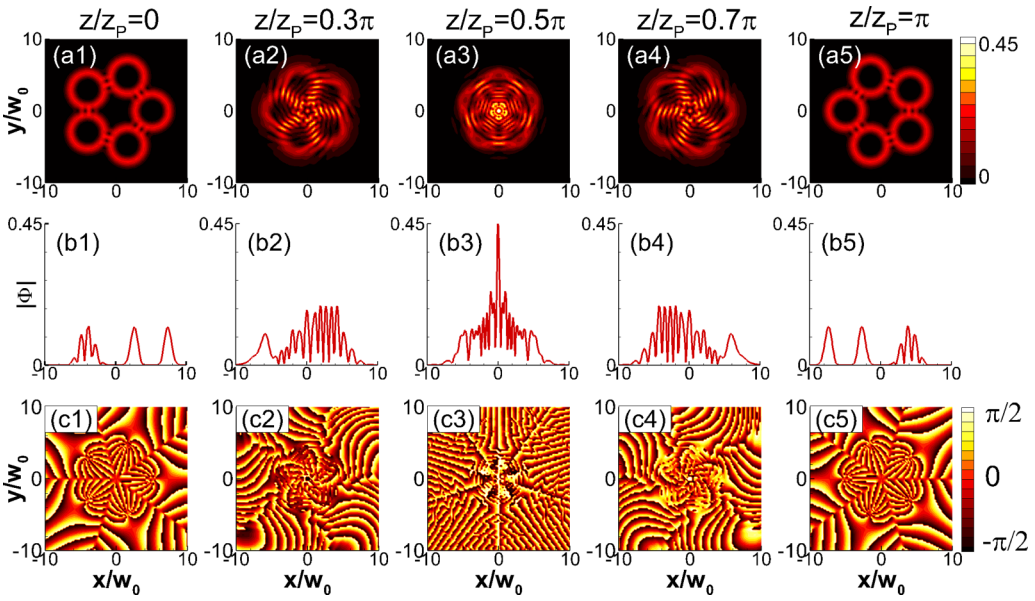

FIG. 6. The same as Fig. 5 except that $m = 5$.

light intensity is no longer zero during propagation, as seen by comparing the rotations in Figs. 5(b) and 6(b). The bright-and-dark fringes result from the constructive and destructive interferences of the superimposed light field. According to the interference theory, the appearance of each interference fringe is due to the phase difference of 2π between two coherent beams. It is well known that the phase of a vortex beam field has a helical phase variation of an integer multiple of 2π around the vortex core. m is the very number of 2π phase cycles around the optical vortex centered on each constituent AVB, as shown in Figs. 5(c) and 6(c). It governs the vortex nature of the array field through the phase factor $\exp(-im\theta)$. For a vortex beam with topological charge of m, there will be a wavefront phase change of $2\pi m$ accompanying every rotation of the azimuth angle. If we consider the ringlike array consisting of N vortex beams as a single beam, the azimuthal angle of the ringlike array rotates one cycle, and the phase change of $2\pi mN$ will occur.

Figure 7 graphs the transverse intensity distributions of the AVB arrays with topological charge from $m = 0$ to 9, respectively, for comparison. We take the intensity patterns at $z = 0.3\pi z_p$ as an example to illustrate its regularity of change. One sees that the intensity profile is a peak at $x = 0$ only when $m = 0$ and 5, while the intensity profile is a valley at $x = 0$ when m takes other values. This corresponds to the fact that the central light intensity is not zero when $m = 0$ and 5 but it is always zero when m takes other values. Moreover, through more numerical simulations, we find that the central light intensity of the AVB arrays, in the case of in-phase incidence, is not zero only if the ratio m/N is an integer. To put it another way, the dark core of the array field exists throughout the propagation process if the ratio m/N is not an integer. At

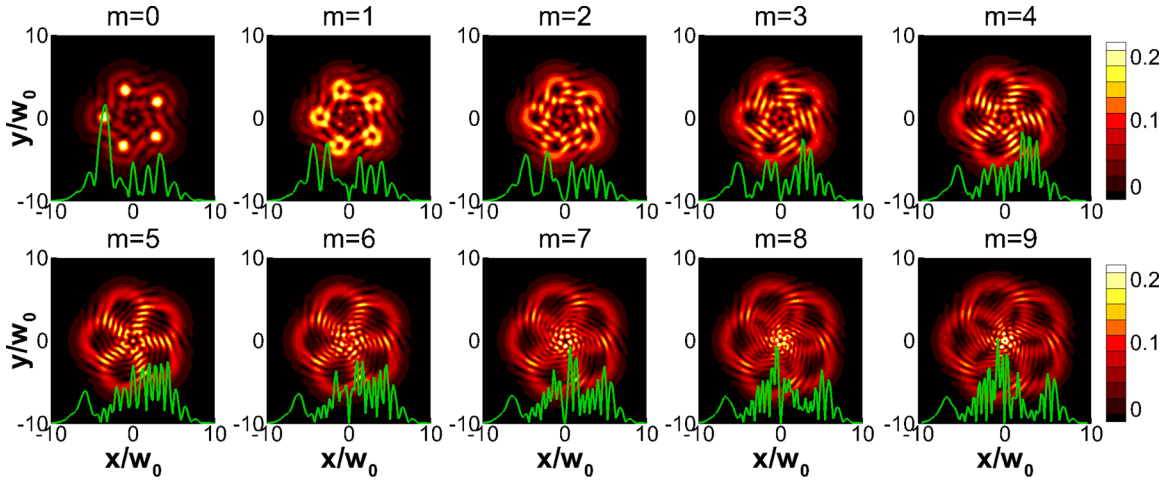

FIG. 7. Transverse intensity patterns of the AVB array with different numbers of topological charge m at the same propagation position $z = 0.3\pi z_p$; the insets (solid line in each figure) are intensity profiles of the AVB array in the x direction. Parameters: $N = 5$, $n = 3$, $r = 5w_0$, $\xi = 1/2$, $P_0 = P_{gc}/5$.

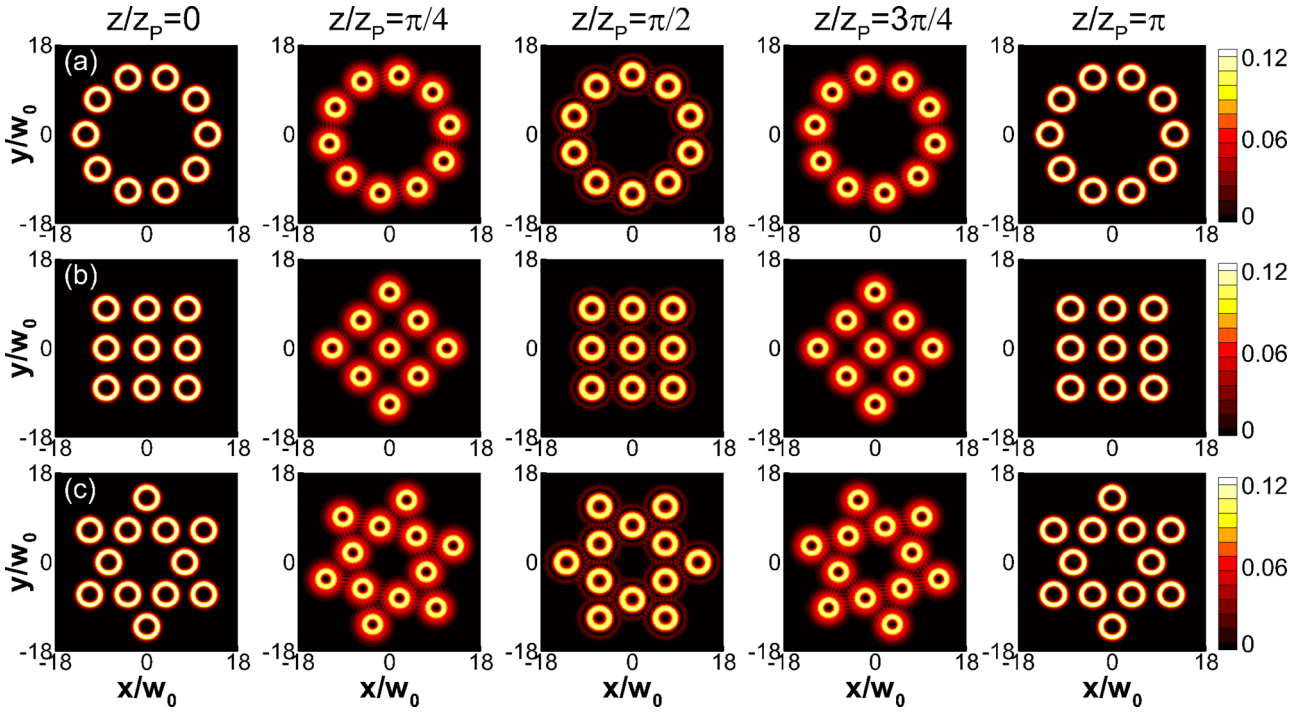

FIG. 8. Examples of the spiraling AVB arrays. Common parameters: $m = n = 3$, $P_0 = P_{gc}/5$, $\xi = 1$. Respective parameters: (a) $N = 10$, $r = 12w_0$; (b) $N_s = 9$, $r = 8w_0$; (c) $N_s = 12$, $r = 7.5w_0$. The subscript s of N means *sum*.

the same propagation position, the greater the value of m, the greater the number of light intensity peaks. Of course, it is inseparable from the diffraction effect of each constituent AVB and the nonlinear effect of the medium, which cause the superposition of optical fields between neighboring beams.

C. Other array forms

In the past, there have been many studies on single-beam [34–36,40,47], double-beam [6,44,48], and ringlike beam arrays [28,29], but relatively few on other types of beam arrays. Here, we give more forms of multibeam interaction.

To verify the model of our spiraling arrays, we perform a series of simulations of different N values, as shown in Fig. 8. In view of the importance of the dynamical bound state (array soliton), we only give the case of $\xi = 1$. The spiraling necklacelike, square-matrix-like, and polygonlike fields can be obtained through appropriately designed radius r. The smaller the value of r the tighter is the arrangement of the beam arrays, and the higher the overlap degree between the constituent beams the more concentrated is the energy. In the process of constructing Fig. 8(a), we take the parameters as $N = 10$ and $r = 12w_0$. In the process of constructing Fig. 8(b),

$$N_s = 9 \begin{cases} \text{take } j = 1 & \text{when } N_1 = 1 \quad \text{with } r_1 = 0, \\ \text{take } j = 1, 2, 3, 4 & \text{when } N_2 = 4 \quad \text{with } r_2 = r, \\ \text{take } j = 1, 3, 5, 7 & \text{when } N_3 = 8 \quad \text{with } r_3 = \sqrt{2}r. \end{cases}$$

In the process of constructing Fig. 8(c),

$$N_s = 12 \begin{cases} \text{take } j = 1, 2, 3, 4, 5, 6 & \text{when } N_1 = 6 \quad \text{with } r_1 = r, \\ \text{take } j = 1, 3, 5, 7, 9, 11 & \text{when } N_2 = 12 \quad \text{with } r_2 = \sqrt{3}r. \end{cases}$$

Also, many other desirable fields can be obtained by selecting appropriate incident parameters. They can be regarded as generalized high-order spatial soliton forms. The shape of the array field remains invariant during propagation and rotates with the period $2\pi z_p$. Each constituent AVB revolves both around the center of mass of the arrays (i.e., the propagation axis) and on its own axis. If we assume that the constituent beams do not travel along the z axis, and the propagation distance z is regarded as time t, then their motion is confined in the x-y plane. In this case, the orbits of the AVBs are concentric circles. Of course, elliptical orbits can also be realized; at this point, the beam array propagates as array breathers. Each constituent beam undergoes alternating transformation of dispersion and aggregation during propagation, as discussed earlier in Fig. 1.

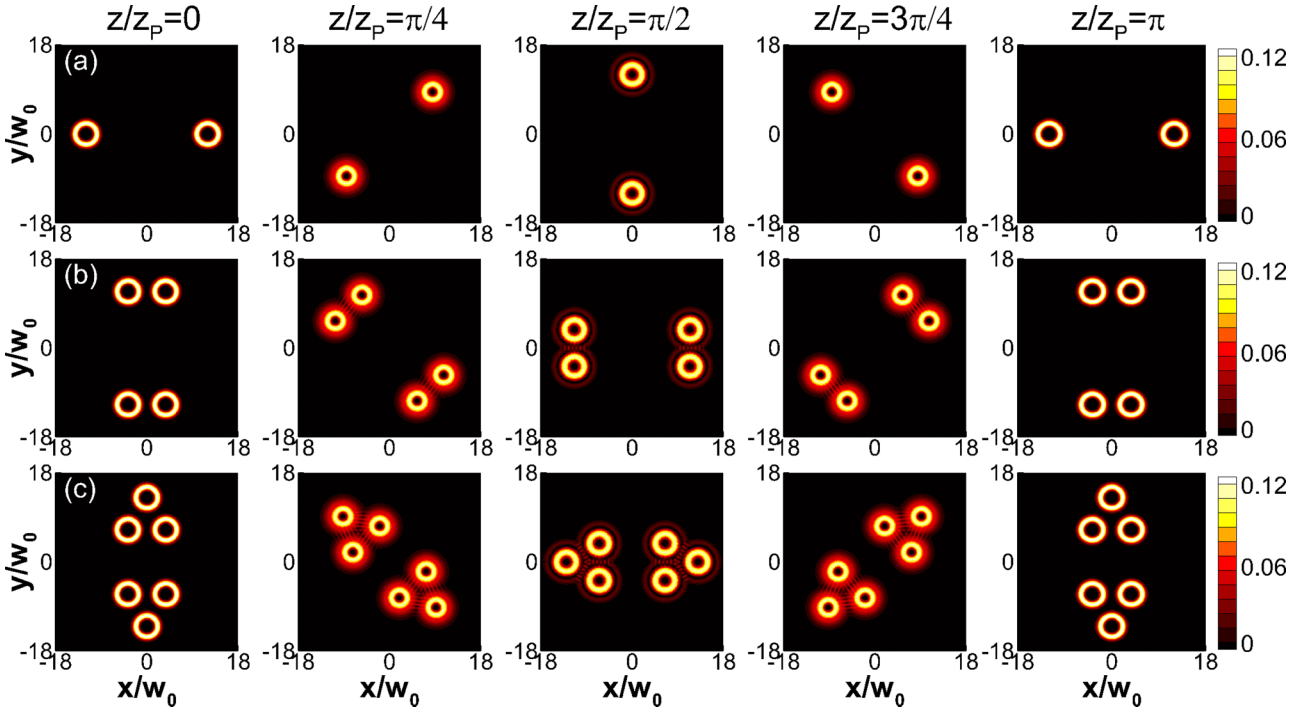

FIG. 9. Examples of the spiraling AVB arrays. Common parameters: $m = n = 3$, $P_0 = P_{gc}/5$, $\xi = 1$. Respective parameters: (a) $N_s = 2$, where we take constituent beams represented by $j = 5, 10$ when $N = 10$ with $r = 12w_0$; (b) $N_s = 4$, where we take constituent beams represented by $j = 2, 3, 7, 8$ when $N = 10$ with $r = 12w_0$; (c) $N_s = 6$, where we take constituent beams represented by $j = 1, 2, 4, 5$ when $N_1 = 6$ with $r_1 = r$ and by $j = 3, 9$ when $N_2 = 12$ with $r_2 = \sqrt{3}r$, $r = 7.5w_0$.

Taking our model one step further, the array soliton pairs [Fig. 9(a)] and array soliton groups [Figs. 9(b) and 9(c), each soliton group consisting of two, three, or even more solitons] can be constructed. They can all evolve from the simplest ringlike structure. Certainly, we can regard Figs. 9(b) and 9(c) as rectanglelike and hexagonal-like array fields, respectively. Each soliton group has a precession motion around the propagation axis at an equal angular velocity $\omega(z) = 1/z_p$. The spacing between the center of mass of the two soliton groups in Figs. 9(a)–9(c) can be obtained as

$$D_a(z) = 2d(z), \tag{41}$$

$$D_b(z) = 2\cos(\pi/10)d(z), \tag{42}$$

$$D_c(z) = (4\sqrt{3}/3)d(z), \tag{43}$$

respectively. It can be verified that Eqs. (41)–(43) are valid when $\xi \neq 1$. This provides a theoretical model for simultaneous transmission of multiple groups of signals without interfering with each other. For an actual medium with fixed length L, the coordinate of each signal at the exit plane can be separately written as $(x_{cj}(L), y_{cj}(L))$. Similarly, the length of the medium can be determined according to the output position of the signal and the initial incident conditions. In this respect, these models have potential applications in optical communication and particle control. No more multibeam interaction forms are given here, but the interested reader can establish them according to the approach provided in this paper.

IV. CONCLUSION

A class of spiraling AVB arrays has been introduced, the propagation expression of the beam array in SNNM has been derived, and the propagation properties have been analyzed analytically and by numerical simulations. Such arrays, which can be viewed as a generalized single beam, present more unique forms of propagation and transformation. We roughly divide the propagation state of the beam array into three situations (shrink, expansion, and dynamical bound state) based on the introduced transverse velocity parameter. Two concepts—the array soliton (the shape and size of the array do not change during propagation) and the array breather (at least one of the shape and size of the array changes during propagation)—are proposed based on our model. Although each constituent AVB rotates as an individual around its respective beam center, all the beams are in a synchronous motion during propagation. In this regard, the spiraling beam array may act as a powerful tool for dynamic control over multiple particles. In view of the increasing interest in the optical vortices, it is hoped that our result will provide a broader basis for further research into the interaction of the vortex beam arrays. Our results may have potential applications in optical communication, particle manipulation, and other related fields.

Here, we give a short discussion about the related physical generation of input beams needed to observe the spiraling AVB arrays. The experimental generation of a single AVB has been reported in Ref. [21]. In terms of the formation of beam arrays, the experimental setup mentioned in Ref. [49] (which can generate beam arrays with controllable beam

order and spatial distributions) may be helpful, and also the modified holographic beam shaping technique mentioned in Ref. [22].

ACKNOWLEDGMENTS

This research was supported by the National Natural Science Foundation of China (Grants No. 61308016, No. 11374089, and No. 61605040), the Chunhui Plan of Ministry of Education of China (Grant No. Z2017020), the Natural Science Foundation of Hebei Province (Grants No. F2017205060, No. F2017205162, and No. F2016205124), the Technology Key Project of Colleges and Universities of Hebei Province (Grant No. ZD2018081), the Science Fund for Distinguished Young Scholars of Hebei Normal University (Grant No. L2017J02), and the Innovation Project of Graduate School of Hebei Normal University (Grant No. CXZZSS2019069).

[1] M. Peccianti, K. A. Brzdakiewicz, and G. Assanto, Nonlocal spatial soliton interactions in nematic liquid crystals, Opt. Lett. **27**, 1460 (2002).

[2] C. Conti, M. Peccianti, and G. Assanto, Observation of Optical Spatial Solitons in a Highly Nonlocal Medium, Phys. Rev. Lett. **92**, 113902 (2004).

[3] C. Rotschild, O. Cohen, O. Manela, M. Segev, and T. Carmon, Solitons in Nonlinear Media with an Infinite Range of Nonlocality: First Observation of Coherent Elliptic Solitons and of Vortex-Ring Solitons, Phys. Rev. Lett. **95**, 213904 (2005).

[4] C. Rotschild, M. Segev, Z. Y. Xu, Y. V. Kartashov, L. Torner, and O. Cohen, Two-dimensional multipole solitons in nonlocal nonlinear media, Opt. Lett. **31**, 3312 (2006).

[5] S. Zeng, M. Chen, T. Zhang, W. Hu, Q. Guo, and D. Lu, Analytical modeling of soliton interactions in a nonlocal nonlinear medium analogous to gravitational force, Phys. Rev. A **97**, 013817 (2018).

[6] A. W. Snyder and D. J. Mitchell, Accessible solitons, Science **276**, 1538 (1997).

[7] Q. Guo, B. Luo, F. Yi, S. Chi, and Y. Xie, Large phase shift of nonlocal optical spatial solitons, Phys. Rev. E **69**, 016602 (2004).

[8] D. Lu, Q. Zhan, Q. Duan, and W. Hu, Power-variation-induced three-dimensional nonuniform scaling of beams in strongly nonlocal nonlinear media, Phys. Rev. A **87**, 023815 (2013).

[9] Q. Kong, M. Shen, Z. Chen, Q. Wang, R. K. Lee, and W. Krolikowski, Dark solitons in nonlocal media with competing nonlinearities, Phys. Rev. A **87**, 063832 (2013).

[10] Z. Shi, Q. Guo, and H. Li, Helmholtz bright soliton splitting at nonlocal nonlinear interfaces, Phys. Rev. A **88**, 063848 (2013).

[11] Y. Zheng, Y. Gao, J. Wang, F. Lv, D. Lu, and W. Hu, Bright nonlocal quadratic solitons induced by boundary confinement, Phys. Rev. A **95**, 013808 (2017).

[12] D. Lu, W. Hu, Y. Zheng, Y. Liang, L. Cao, S. Lan, and Q. Guo, Self-induced fractional Fourier transform and revivable higher-order spatial solitons in strongly nonlocal nonlinear media, Phys. Rev. A **78**, 043815 (2008).

[13] D. Lu and W. Hu, Theory of multibeam interactions in strongly nonlocal nonlinear media, Phys. Rev. A **80**, 053818 (2009).

[14] Z. Liu, Y. Liu, Y. Ke, Y. Liu, W. Shu, H. Luo, and S. Wen, Generation of arbitrary vector vortex beams on hybrid-order Poincaré sphere, Photonics Res. **5**, 15 (2017).

[15] X. Ma and S. Schumacher, Vortex-vortex control in exciton-polariton condensates, Phys. Rev. B **95**, 235301 (2017).

[16] X. Ma and S. Schumacher, Vortex Multistability and Bessel Vortices in Polariton Condensates, Phys. Rev. Lett. **121**, 227404 (2018).

[17] Y. Yang, G. Thirunavukkarasu, M. Babiker, and J. Yuan, Orbital-Angular-Momentum Mode Selection by Rotationally Symmetric Superposition of Chiral States with Application to Electron Vortex Beams, Phys. Rev. Lett. **119**, 094802 (2017).

[18] A. E. Willner, L. Li, G. Xie, Y. Ren, H. Huang, Y. Yue, N. Ahmed, M. J. Willner, A. J. Willner, Y. Yan, Z. Zhao, Z. Wang, C. Liu, M. Tur, and S. Ashrafi, Orbital-angular-momentum-based reconfigurable optical switching and routing, Photonics Res. **4**, B5 (2016).

[19] Z. Zhuang, D. Deng, X. Chen, F. Zhao, X. Peng, D. Li, and L. Zhang, Spatiotemporal sharply autofocused dual-Airy-ring Airy Gaussian vortex wave packets, Opt. Lett. **43**, 222 (2018).

[20] X. Ma, O. A. Egorov, and S. Schumacher, Creation and Manipulation of Stable Dark Solitons and Vortices in Microcavity Polariton Condensates, Phys. Rev. Lett. **118**, 157401 (2017).

[21] Y. Yang, Y. Dong, C. Zhao, and Y. Cai, Generation and propagation of an anomalous vortex beam, Opt. Lett. **38**, 5418 (2013).

[22] L. Li, C. Chang, X. Yuan, C. Yang, S. Feng, S. Nie, and J. Ding, Generation of optical vortex array along arbitrary curvilinear arrangement, Opt. Express **26**, 9798 (2018).

[23] Y. Yan, G. Xie, M. P. J. Lavery, H. Huang, N. Ahmed, C. Bao, Y. Ren, Y. Cao, L. Li, Z. Zhao, A. F. Molisch, M. Tur, M. J. Padgett, and A. E. Willner, High-capacity millimetre-wave communications with orbital angular momentum multiplexing, Nat. Commun. **5**, 4876 (2014).

[24] M. Padgett and R. Nowman, Tweezers with a twist, Nat. Photonics **5**, 343 (2011).

[25] M. Shih and M. Segev, Three-Dimensional Spiraling of Interacting Spatial Solitons, Phys. Rev. Lett. **78**, 2551 (1997).

[26] V. V. Steblina, Yu. S. Kivshar, and A. V. Buryak, Scattering and spiraling of solitons in a bulk quadratic medium, Opt. Lett. **23**, 156 (1998).

[27] D. Buccoliero, A. S. Desyatnikov, W. Krolikowski, and Y. S. Kivshar, Spiraling multivortex solitons in nonlocal nonlinear media, Opt. Lett. **33**, 198 (2008).

[28] A. S. Desyatnikov and Y. S. Kivshar, Rotating Optical Soliton Clusters, Phys. Rev. Lett. **88**, 053901 (2002).

[29] Y. V. Kartashov, L. C. Crasovan, D. Mihalache, and L. Torner, Robust Propagation of Two-Color Soliton Clusters Supported by Competing Nonlinearities, Phys. Rev. Lett. **89**, 273902 (2002).

[30] D. Buccoliero, A. S. Desyatnikov, W. Krolikowski, and Y. S. Kivshar, Laguerre and Hermite Soliton Clusters in Nonlocal Nonlinear Media, Phys. Rev. Lett. **98**, 053901 (2007).

[31] A. Fratalocchi, A. Piccardi, M. Peccianti, and G. Assanto, Nonlinearly controlled angular momentum of soliton clusters, Opt. Lett. **32**, 1447 (2007).
[32] A. V. Buryak, Y. S. Kivshar, M. Shih, and M. Segev, Induced Coherence and Stable Soliton Spiraling, Phys. Rev. Lett. **82**, 81 (1999).
[33] A. V. Buryak, V. V. Steblina, Soliton collisions in bulk quadratic media: Comprehensive analytical and numerical study, J. Opt. Soc. Am. B **16**, 245 (1999).
[34] D. Deng and Q. Guo, Propagation of Laguerre-Gaussian beams in nonlocal nonlinear media, J. Opt. A **10**, 035101 (2008).
[35] Z. J. Yang, S. M. Zhang, X. L. Li, and Z. G. Pang, Variable sinh-Gaussian solitons in nonlocal nonlinear Schrödinger equation, Appl. Math. Lett. **82**, 64 (2018).
[36] G. Liang, W. Cheng, Z. Dai, T. Jia, M. Wang, and H. Li, Spiraling elliptic solitons in lossy nonlocal nonlinear media, Opt. Express **25**, 11717 (2017).
[37] G. Liang and Q. Guo, Spiraling elliptic solitons in nonlocal nonlinear media without anisotropy, Phys. Rev. A **88**, 043825 (2013).
[38] J. Wyller, W. Krolikowski, O. Bang, and J. J. Rasmussen, Generic features of modulational instability in nonlocal Kerr media, Phys. Rev. E **66**, 066615 (2002).
[39] J. Arnaud, *Beam and Fibre Optics* (Academic, New York, 1976).
[40] Y. Cai, X. Lu, and Q. Lin, Hollow Gaussian beams and their propagation properties, Opt. Lett. **28**, 1084 (2003).
[41] Z. Yang, D. Lu, W. Hu, Y. Zheng, X. Gao, and Q. Guo, Propagation of optical beams in strongly nonlocal nonlinear media, Phys. Lett. A **374**, 4007 (2010).
[42] A. Erdelyi, W. Magnus, and F. Oberhettinger, *Tables of Integral Transforms* (McGraw-Hill, New York, 1954).
[43] Z. Dai, Z. Yang, X. Ling, S. Zhang, and Z. Pang, Interaction trajectory of solitons in nonlinear media with an arbitrary degree of nonlocality, Ann. Phys. **366**, 13 (2016).
[44] Z. J. Yang, Z. F. Yang, J. X. Li, Z. P. Dai, S. M. Zhang, and X. L. Li, Interaction between anomalous vortex beams in nonlocal media, Results Phys. **7**, 1485 (2017).
[45] Z. Dai, Z. Yang, S. Zhang, and Z. Pang, Propagation of anomalous vortex beams in strongly nonlocal nonlinear media, Opt. Commun. **350**, 19 (2015).
[46] G. P. Agrawal, *Nonlinear Fiber Optics*, 5th ed. (Academic, New York, 2013).
[47] Y. J. He, B. A. Malomed, D. Mihalache, and H. Z. Wang, Crescent vortex solitons in strongly nonlocal nonlinear media, Phys. Rev. A **78**, 023824 (2008).
[48] Z. Shi, J. Xue, X. Zhu, Y. Xiang, and H. Li, Interaction of Airy-Gaussian beams in photonic lattices with defects, Phys. Rev. E **95**, 042209 (2017).
[49] C. Liang, X. Zhu, C. Mi, X. Peng, P. Wang, Y. Cai, and S. A. Ponomarenko, High-quality partially coherent Bessel beam array generation, Opt. Lett. **43**, 3188 (2018).